Scanning Localized Magnetic Fields in a Microfluidic Device with a Single Nitrogen Vacancy Center

Kangmook Lim,[†,‡] Chad Ropp,[†] Benjamin Shapiro,[§] Jacob M. Taylor,[‡] and Edo Waks*[,†,‡]

[†]Department of Electrical and Computer Engineering and Institute for Research in Electronics and Applied Physics, University of Maryland, College Park, Maryland 20742, United States
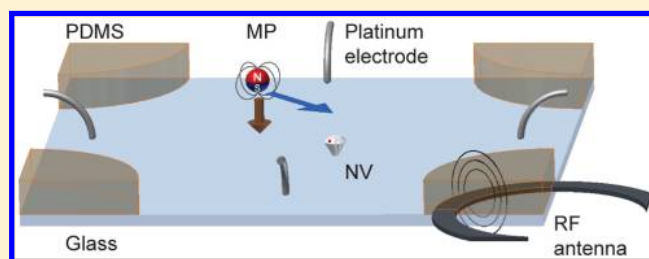
[‡]Joint Quantum Institute, University of Maryland and the National Institute of Standards and Technology, College Park, Maryland 20742, United States

[§]Fischell Department of Bioengineering and the Institute for Systems Research, University of Maryland, College Park, Maryland 20742, United States

Ⓢ *Supporting Information*

ABSTRACT: Nitrogen vacancy (NV) color centers in diamond enable local magnetic field sensing with high sensitivity by optical detection of electron spin resonance (ESR). The integration of this capability with microfluidic technology has a broad range of applications in chemical and biological sensing. We demonstrate a method to perform localized magnetometry in a microfluidic device with a 48 nm spatial precision. The device manipulates individual magnetic particles in three dimensions using a combination of flow control and magnetic actuation. We

map out the local field distribution of the magnetic particle by manipulating it in the vicinity of a single NV center and optically detecting the induced Zeeman shift with a magnetic field sensitivity of 17.5 μT Hz$^{-1/2}$. Our results enable accurate nanoscale mapping of the magnetic field distribution of a broad range of target objects in a microfluidic device.

KEYWORDS: *nitrogen vacancy (NV) color centers, diamond nanocrystal, electron spin resonance (ESR), localized magnetometry, microfluidic device, magnetic particles*

Nitrogen vacancy (NV) color centers in diamond possess remarkable properties that include single photon emission,[1,2] a spin-triplet ground state with long spin coherence time at room temperature,[3,4] and spin dependent photoluminescence.[5,6] These properties enable highly sensitive NV-based magnetic field sensors with nanoscale spatial precision,[7−11] in contrast to other types of magnetic field sensors that achieve excellent field sensitivity but whose size is typically on the order of tens of microns or larger.[12−14] NV magnetometry has been deployed in a variety of applications such as detection of nanomechanical oscillations,[15] readout of magnetic data,[16,17] monitoring ion concentrations,[18−20] and magnetic imaging.[21,22] NV centers in diamond are also biocompatible[23−25] and, thus, can serve as biological sensors.[26−28] This capability has motivated recent efforts to manipulate and control a diamond nanocrystal hosting an ensemble of NV centers[29] and a single NV center[30] in a liquid environment using optical trapping techniques.

The integration of NV magnetometry with microfluidic systems could open up new possibilities for real-time biological and chemical sensing. Microfluidics provides an ideal device platform for sorting and manipulating samples using magnetic, optical, mechanical, or electrical methods.[31,32] An important recent example is the work of Steinert et al.[33] that demonstrated a spin relaxometry technique based on an array of NV centers in a microfluidic device. This technique measured the concentration of a large ensemble of freely diffusing magnetic ions and molecules.

However, the microfluidic device in that work was only used to prepare appropriate ion concentrations.

In addition to preparing fluid concentrations, microfluidics can also isolate and manipulate individual objects. For example, a variety of control methods based on electrokinetic[34−36] and magnetic tweezers[37−39] can manipulate objects inside a microfluidic device with nanometer spatial precision.[40−42] Combining these highly precise particle manipulation approaches with NV magnetometry opens up the possibility to map the magnetic field distributions of target objects with nanoscale accuracy, which is essential for a broad range of magnetic imaging applications.[7,8]

Here, we demonstrate the ability to map the magnetic field of suspended objects in a microfluidic system with high nanometer spatial resolution and high sensitivity using NV magnetometry. We manipulate a single magnetic particle in three dimensions using a combination of planar electroosmotic flow control and vertical magnetic actuation. A diamond nanocrystal containing a single NV color center acts as a localized magnetic field sensor for the manipulated magnetic particle. We measure the magnetic field generated by the magnetic particle via optically detected electron spin resonance (ESR) measurements and map out its
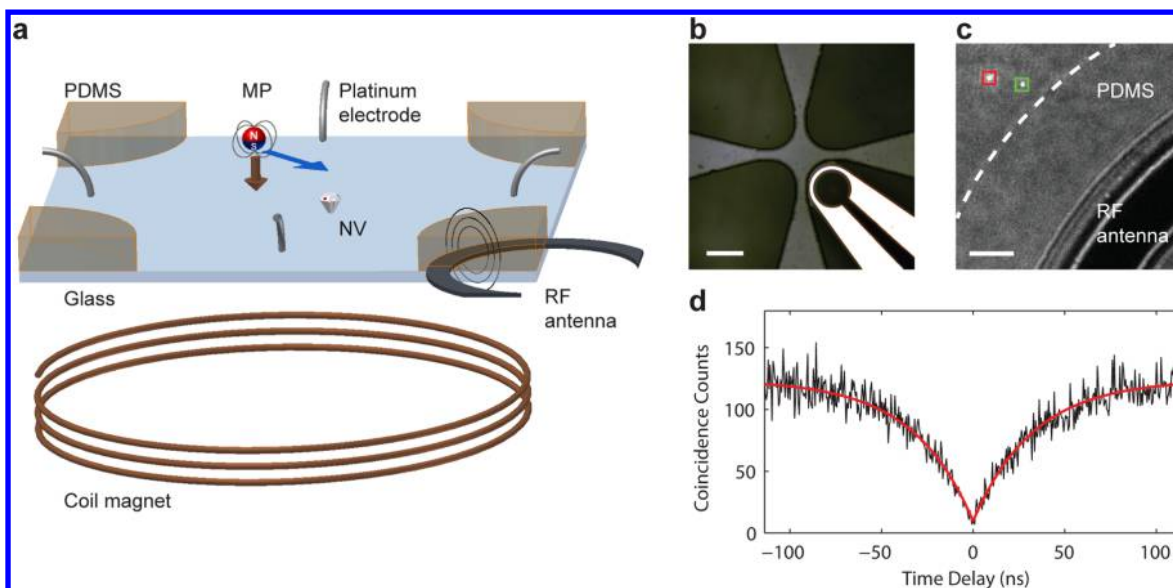
Figure 1. (a) Schematic of microfluidic device used to implement NV magnetometry. The magnetic particle is labeled by "MP". (b) Optical image of the control chamber of the microfluidic device along with integrated microwave antenna. Scale bar is 100 μm. (c) EM-CCD image of an immobilized NV center (green) and a suspended magnetic particle (red) inside the microfluidic control chamber. The white dashed line represents the boundary between the fluid and the PDMS sidewall of the channel. Scale bar is 5 μm. (d) Second order correlation measurement of a single NV center in a diamond nanocrystal.

field distribution with nanoscale accuracy. In contrast to other scanning magnetometry methods based on AFM,[9,16] which require complex experimental setup and are challenging to perform in liquids, our approach uses only simple optical microscopy and is naturally integrated into a microfluidic device. Our results thus open up the possibility for highly sensitive mapping of local magnetic field distributions in a fluid environment.

Figure 1a illustrates the microfluidic system we have developed to manipulate magnetic particles and perform localized magnetometry. The device is composed of two microfluidic channels formed between a glass coverslip (1 in. × 1 in. wide, 150 μm thick) and a molded block of polydimethylsiloxane (PDMS). The microfluidic channels are filled with a viscous fluid that contains target magnetic particles in a liquid suspension (see Supporting Information). In addition to increasing the fluid viscosity, the fluid also serves to push the magnetic particles to the surfaces of the device.[41,42] We find that the magnetic particles are preferably confined at the top PDMS surface of the microfluidic channels. The intersection between the two channels forms the control chamber where we manipulate particles and map their magnetic field distribution.

We manipulate particles in the plane of the microfluidic device by applying voltages at the four ends of the microfluidic channels and using feedback control.[40−42] The voltages induce electroosmotic flow that moves the suspended magnetic particle toward desired directions by viscous drag (see Supporting Information). To achieve vertical manipulation, we use magnetic actuation. We place a coil magnet under the microfluidic device that applies a magnetic field in the vertical direction. The magnetic field provides a downward force on the magnetic particle and also orients its dipole moment along the vertical direction.

In order to perform local magnetometry, we deposit a dilute concentration of diamond nanocrystals (mean size of 25 nm) on the glass surface of the microfluidic device using a spin coating method. These diamond nanocrystals serve as local magnetic field sensors. We lithographically pattern a microwave antenna (500 nm Au, 10 nm Ti) on the glass coverslip surface in order to

drives the spin transition of the NV center to perform optically detected ESR measurements.[7] Figure 1b shows an optical image of the microfluidic device with the integrated microwave antenna. We align the microfluidic channel such that the microwave antenna is as close as possible to the control chamber without directly penetrating into it. A tunable microwave signal generator (ROHDE&SCHWARZ SMC100A) drives the antenna over a spectral range that spans the entire ESR resonance of the NV center (centered at 2.863 GHZ).

We mount the microfluidic device on a confocal microscope that excites the sample and collects emission (see Supporting Information). Figure 1c shows an EM-CCD camera image of a single diamond nanocrystal and a nearby magnetic particle in the control chamber of the microfluidic device. For all experiments reported in this letter the magnetic particles are spherical maghemite magnetic beads with a radius of 500 nm (Chemicell, Germany). The green and red boxes highlight the diamond nanocrystal and the magnetic particle, respectively. We select a diamond nanocrystal located close to the patterned microwave antenna in order to minimize the microwave power required to excite ESR transitions. Figure 1d shows an autocorrelation measurement taken from the diamond nanocrystal that exhibits clear antibunching, indicating that it contains only a single NV defect (see Supporting Information).

We first investigate the ability to manipulate a magnetic particle within the microfluidic control chamber. Figure 2a−c shows a sequence of camera images of a single magnetic particle that we manipulate on the PDMS surface to undergo a square spiral trajectory using feedback control. The panels show the position of the particle at three different times (150, 300, and 450 s). The cyan and magenta boxes indicate the start and stop positions of the trajectory. The white line shows the past history of the measured positions of the controlled particle.

In order to determine the positioning accuracy we hold the particle at a desired location for 60 s and continuously monitor its position. Figure 2d shows a two-dimensional plot of the measured positions, and Figure 2e,f show position histograms
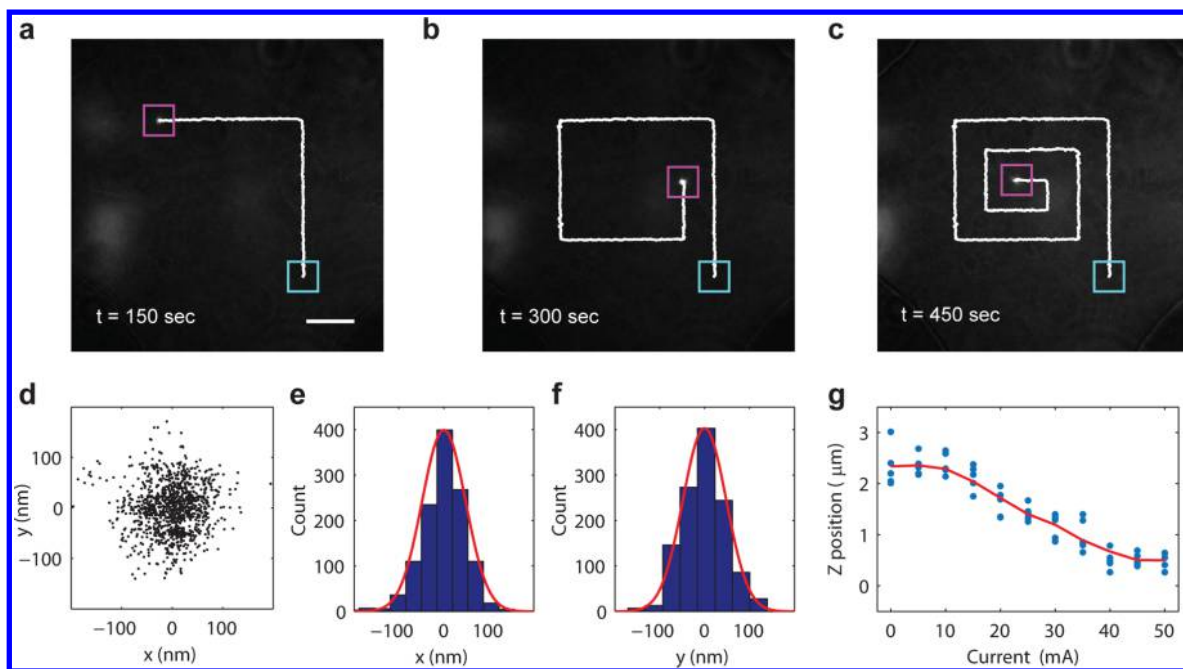
Figure 2. (a−c) Camera images of a magnetic particle manipulated along a 2D square spiral trajectory. The cyan box indicates the start position of the selected magnetic particle, and the magenta boxes indicate the stop location of the particle at 150, 300, and 450 s, respectively. The white line shows the past history of the measured positions. Scale bar is 10 μm. (d) Scatter plots of the measured positions of the magnetic particle held in place using flow control for 60 s. (e, f) Position histograms along the x and y axes of panel d. The solid lines are Gaussian fits to the position histograms. The standard deviation is 48 (47) nm along the x (y) directions, respectively. (g) Vertical distance of the magnetic particle relative to the bottom glass surface as a function of the current driving the coil magnetic underneath the device. Blue dots show individually measured values, whereas the red line shows the averaged values.

along x and y direction, respectively. We fit each histogram to a Gaussian (red solid line) and determine a standard deviation of 48 (47) nm along the x (y) directions, respectively.

To achieve motion of the magnetic particle in the direction orthogonal to the surface, we apply a current to the coil magnet under the device. The generated magnetic field applies a force that pulls the magnetic particle away from the PDMS surface and toward the glass surface. Figure 2g plots the measured distance of the magnetic particle to the bottom glass surface as a function of the current driving the coil magnetic. We measure this distance by sweeping the particle through the focus of the objective lens using the piezo stage that holds the microfluidic device. We determine the focused position from the minimum spot size and record the stage travel distance. We repeat the measurement five times for each value of the external current. The blue dots in Figure 2g show the values obtained for the five individual measurements, whereas the red line shows the average value of the data.

At each driving current, the magnetic particle stabilizes at a different distance relative to the bottom glass surface due to cancellation between fluid forces that push the particle upward to the top PDMS surface, and magnetic gradient forces that pull it downward toward the bottom glass surface. This interplay between chemical buoyancy versus magnetic downward force enables us to control the vertical position of the magnetic particle relative to the device surface. At 40 mA current, the particle is pulled almost all the way to the bottom glass surface. The applied magnetic field also serves to orient the dipole moment of the suspended magnetic particle along the direction of the applied field in the fluid, thereby eliminating the effect of tumbling of the particle that would otherwise randomize its orientation relative to the measurement direction of the NV center.

In order to measure the magnetic field generated by the magnetic particle, we scan its position relative to the NV center and perform optically detected ESR measurements. We isolate a diamond nanocrystal that contains a single NV center on the glass surface in the control chamber. We apply a 50 mA current to the external coil magnet in order to pull the magnetic particle down to the glass surface where the NV center is located. Based on this current and the measurement results in Figure 2g, we estimate the center of the magnetic particle to be located 0.7 μm above the glass surface. Under these conditions, we scan the magnetic particles position relative to the NV center and obtain an ESR spectrum at each position.

We perform the ESR measurements using a digital lock-in approach, as originally proposed by Horowitz et al.[29] (see Supporting Information). This technique eliminates photoluminescence intensity fluctuations that arise slow mechanical drift of the NV center relative to the tight Gaussian excitation laser, instability of the NV center emission caused by charge fluctuations on the surface,[29,43] and other slow intensity fluctuations induced by the microfluidic environment. We perform lock-in by modulating the microwave power supply on and off at a 1 kHz rate and measuring photoluminescence intensity synchronized with this modulation. We define the photoluminescence intensity contrast of the NV center as

$$C(f) = \frac{N_{on}(f) - N_{off}(f)}{N_{off}(f)} \tag{1}$$

where N_{on} and N_{off} are the measured photon counts when the microwave is on and off, respectively, at each value of the microwave frequency.

Figure 3 shows the ESR spectrum of the NV center taken at three different positions of the magnetic particle (see Supporting Information). The left panels show the measured ESR spectrum,
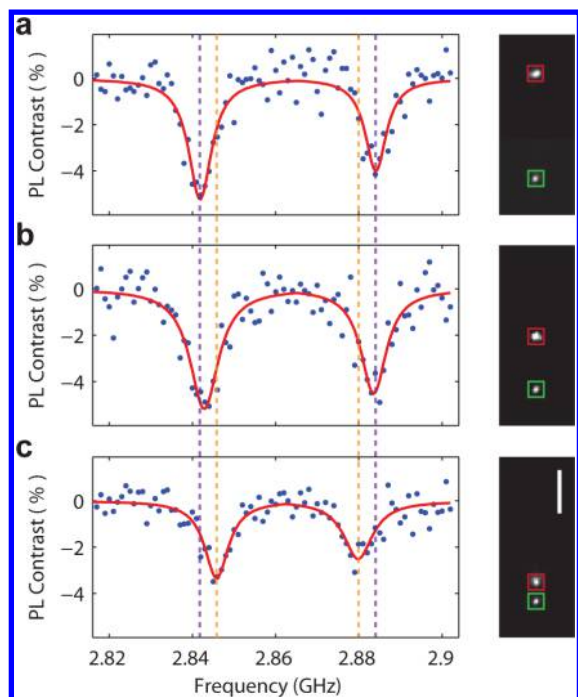
Figure 3. Optically detected ESR spectra (left) and camera images (right) of the magnetic particle (red square) and NV emission (green square) when the particle is at a distance of (a) 7.25 μm, (b) 3.62 μm, (c) and 1.50 μm from the NV center. Scale bar is 3 μm. The red lines in the spectra are Lorentzian fits to measurement data. Dashed lines in purple and orange are the center frequencies of the Lorentzian fits in (a) and (c).

where blue dots represent measured data points and the red lines are Lorentzian fits to the measured data. The right panels show EM-CCD camera images that indicate the horizontal position of the magnetic particle (red box) and the NV center (green box).

Panel a shows the case where the magnetic particle is 7.25 μm away from the NV center so that its contribution to the total magnetic field is negligible. The two ESR peaks correspond to the Zeeman split spin ground states of the NV center which are separated by 42.3 MHz. This large splitting is due to the applied magnetic field from the external coil magnet. As we bring the magnetic particle to a distance of 3.62 μm (panel b), the Zeeman splitting reduces to 40.7 MHz because the field generated by the magnetic particle opposed the external field of the coil magnet. This change in Zeeman splitting provides a direct quantitative measure of the magnetic field given by the magnetic particle. At an even shorter distance of 1.50 μm (panel c), the Zeeman splitting is further reduced to 34.2 MHz.

To determine the measurement noise, we calculate the average root-mean-square fluctuations of the data in Figure 3a (relative to the fitted curve) to be 0.66%, which is very close to the 0.6% fluctuations predicted by shot noise (see Supporting Information). The noise fluctuations can be compared to the PL intensity contrast of 5.2% at ESR resonance determined from the Lorentzian fitting, which corresponds to a signal noise ratio (SNR) of 7.8. This SNR is reasonably consistent with other measurements of single NV centers in a fluid environment.[30]

Because our system operates close to the shot noise limit, we can estimate the magnetic field sensitivity of our magnetometry system using the shot-noise limited relation[7,44]

$$\eta_{\text{B}} = 0.77 \frac{h}{g\mu_{\text{B}}} \frac{\Delta\nu}{C\sqrt{R}} \tag{2}$$

where h is the Planck constant, $g = 2$ is the Lande g-factor for the NV center, and μ_{B} is the Bohr magneton. Using the data in Figure 3a, we calculate a maximum photoluminescence intensity contrast of $C = 0.053$, along with a hyperfine unresolved microwave ESR line width of $\Delta\nu = 7.2$ MHz. The fluorescence count rate is measured to be $R = 45$ kCts/s. Inserting these values into eq 2 we attain an estimated magnetic field sensitivity of 17.5 μT Hz$^{-1/2}$. This result compares well with previously reported magnetic field sensitivities of NV magnetometry demonstrated in a liquid environment.[29,30]

Our measurement sensitivity could potentially be impacted by various fluctuations in the microfluidic environment that include tumbling of the magnetic particle and temperature fluctuations induce by microwave heating of the fluid. We observe the Zeeman splitting due to the induced field from the magnetic particle in Figure 3. These results rule out the possibility that the magnetic particle is tumbling significantly, and indicate that the applied external magnetic field strongly orients the particle in a fixed direction. A tumbling magnetic particle would make the ESR spectrum broaden, not change the Zeeman splitting.[29] We also calculate the center frequency between the two resonances to be 2.863 MHz in all three cases indicating that we do not observe a heat induced shift due to microwave excitation. A temperature increase would shift both resonances in the same direction and thus change the ESR center frequency,[28,45,46] but would not significantly affect the Zeeman splitting.

We note that the contrast of the ESR spectrum is reduced in Figure 3c as compared with 3a. We attribute this reduction in contrast to increased background from scattering of the white light source by the magnetic particle. We observe a photon count rate of 45 kCts/s in Figure 3a, which increases to 75 kCts/s in Figure 3c. Because the NV excitation power remains the same in both measurements, the increased count rate results from the particle being brought closer to the spatial position where we collect light and direct it to the photodiode. Although two spots are well resolved on the camera in Figure 3c, we use a pinhole spatial filter on the photodiode that is slightly larger than the diffraction spot in order to reduce the sensitivity of the system to sample drift. As the particle gets closer to the NV center, it therefore scatters more light through the spatial filter resulting in an increased background level. This background could be eliminated in principle by using a stroboscopic measurement approach that switches the white light on to track and then off to measure with the photodiode.

To map out the magnetic field distribution of the magnetic particle, we position it at various horizontal distances r relative to the NV center and measure the variation in Zeeman splitting. We can approximate the spherical magnetic particle as a magnetic dipole when its radius is small compared to the distance r. Figure 4a plots the calculated magnitude of the magnetic field along the glass surface for a magnetic dipole whose dipole moment points normal to the device surface. The open circles represent positions of the magnetic particle relative to the NV center where we sampled the magnetic field. Figure 4b plots the measured magnetic fields of the magnetic particle, obtained from the change in Zeeman splitting, as a function of distance r. Error bars denote the 95% confidence bound of the Lorentzian fit used to find the center frequencies of the two Zeeman split ESR transitions. The red curve represents the theoretically predicted magnetic field along the glass surface for a point magnetic dipole. In these calculations, we treat the magnitude of the particle's magnetic moment and orientation of the NV center as fitting parameters (see Supporting Information). We note that the
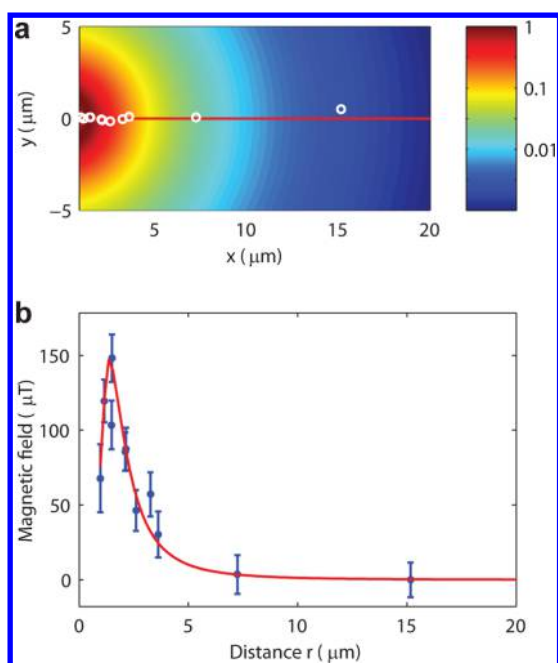
Figure 4. (a) Calculated magnetic field intensity of a magnetic dipole as a function of distance. Open white circles represent experimentally sampled positions of the magnetic field. (b) Measured magnetic field at the various positions represented by the open circles in panel a. Error bars denote the 95% confidence bound of the Lorentzian fit to the ESR spectra. The red curve represents the theoretically calculated magnetic field for the magnetic particle, assumed to be a magnetic dipole.

dipole model is only accurate when the distance of the particle to the NV center exceeds the particle radius (500 nm). This condition is satisfied for virtually all the data points in the figure.

In conclusion, we have developed a microfluidic platform to perform NV magnetometry and map localized magnetic fields of magnetic objects. Our method can be extended to scan any particle that we can image and manipulate by flow, making it highly versatile and largely agnostic to the target being scanned. We can improve the magnetic field sensitivity of our system by using NV centers in fabricated nanocrystals from ultrapure chemical vapor deposition (CVD) diamond, which have longer coherence times,[47,48] and by utilizing pulsed measurement techniques using Ramsey interferometry that can improve the sensitivity down to $nT/Hz^{1/2}$.[7,8] Furthermore, the results reported here using a single NV center can be directly extended to multiple NV centers at different locations of the device surface that serve as parallel sensors for vector magnetometry. They can also be adapted to exploit the electric field[49] and thermal gradient[45,46] sensing capabilities of NV centers to measure other physical parameters. The presented NV magnetometry system could ultimately lead to highly functional microfluidic systems that combine single particle manipulation and real-time sensing to enable a broad range of applications in the study of biological and chemical systems.

■ ASSOCIATED CONTENT

ⓢ Supporting Information
Fluid composition, optical measurement setup, feedback flow control system, ESR spectrum using digital lock-in approach, shot noise limited fluctuations and fitting measured magnetic field to theoretical dipole model. This material is available free of charge via the Internet at http://pubs.acs.org.

■ AUTHOR INFORMATION

Corresponding Author
*E-mail: edowaks@umd.edu.

Notes
The authors declare no competing financial interest.

■ REFERENCES

(1) Kurtsiefer, C.; Mayer, S.; Zarda, P.; Weinfurter, H. *Phys. Rev. Lett.* **2000**, *85*, 290−293.
(2) Beveratos, A.; Brouri, R.; Gacoin, T.; Villing, A.; Poizat, J.-P.; Grangier, P. *Phys. Rev. Lett.* **2002**, *89*, 187901.
(3) Jelezko, F.; Gaebel, T.; Popa, I.; Gruber, A.; Wrachtrup, J. *Phys. Rev. Lett.* **2004**, *92*, 076401.
(4) Balasubramanian, G.; Neumann, P.; Twitchen, D.; Markham, M.; Kolesov, R.; Mizuochi, N.; Isoya, J.; Achard, J.; Beck, J.; Tissler, J.; Jacques, V.; Hemmer, P. R.; Jelezko, F.; Wrachtrup, J. *Nat. Mater.* **2009**, *8*, 383−387.
(5) Gruber, A.; Dräbenstedt, A.; Tietz, C.; Fleury, L.; Wrachtrup, J.; Borczyskowski, C. *Science* **1997**, *276*, 2012−2014.
(6) Manson, N. B.; Harrison, J. P.; Sellars, M. J. *Phys. Rev. B* **2006**, *74*, 104303.
(7) Taylor, J. M.; Cappellaro, P.; Childress, L.; Jiang, L.; Budker, D.; Hemmer, P. R.; Yacoby, A.; Walsworth, R.; Lukin, M. D. *Nat. Phys.* **2008**, *4*, 810−816.
(8) Maze, J. R.; Stanwix, P. L.; Hodges, J. S.; Hong, S.; Taylor, J. M.; Cappellaro, P.; Jiang, L.; Dutt, M. V. G.; Togan, E.; Zibrov, A. S.; Yacoby, A.; Walsworth, R. L.; Lukin, M. D. *Nature* **2008**, *455*, 644−647.
(9) Balasubramanian, G.; Chan, I. Y.; Kolesov, R.; Al-Hmoud, M.; Tisler, J.; Shin, C.; Kim, C.; Wojcik, A.; Hemmer, P. R.; Krueger, A.; Hanke, T.; Leitenstorfer, A.; Bratschitsch, R.; Jelezko, F.; Wrachtrup, J. *Nature* **2008**, *455*, 648−651.
(10) Maertz, B. J.; Wijnheijmer, A. P.; Fuchs, G. D.; Nowakowski, M. E.; Awschalom, D. D. *Appl. Phys. Lett.* **2010**, *96*, 092504.
(11) Schoenfeld, R. S.; Harneit, W. *Phys. Rev. Lett.* **2011**, *106*, 030802.
(12) Gaster, R. S.; Xu, L.; Han, S.-J.; Wilson, R. J.; Hall, D. A.; Osterfeld, S. J.; Yu, H.; Wang, S. X. *Nat. Nano* **2011**, *6*, 314−320.
(13) Li, G.; Joshi, V.; White, R. L.; Wang, S. X.; Kemp, J. T.; Webb, C.; Davis, R. W.; Sun, S. *J. Appl. Phys.* **2003**, *93*, 7557−7559.
(14) Dolabdjian, C.; Qasimi, A.; Bloyet, D.; Mosser, V. *Phys. C (Amsterdam, Neth.)* **2002**, *368*, 80−84.
(15) Arcizet, O.; Jacques, V.; Siria, A.; Poncharal, P.; Vincent, P.; Seidelin, S. *Nat. Phys.* **2011**, *7*, 879−883.
(16) Maletinsky, P.; Hong, S.; Grinolds, M. S.; Hausmann, B.; Lukin, M. D.; Walsworth, R. L.; Loncar, M.; Yacoby, A. *Nat. Nano* **2012**, *7*, 320−324.
(17) Rondin, L.; Tetienne, J.-P.; Spinicelli, P.; Dal Savio, C.; Karrai, K.; Dantelle, G.; Thiaville, A.; Rohart, S.; Roch, J.-F.; Jacques, V. *Appl. Phys. Lett.* **2012**, *100*, 153118.
(18) McGuinness, L. P.; Hall, L. T.; Stacey, A.; Simpson, D. A.; Hill, C. D.; Cole, J. H.; Ganesan, K.; Gibson, B. C.; Prawer, S.; Mulvaney, P. *New J. Phys.* **2013**, *15*, 073042.
(19) Ermakova, A.; Pramanik, G.; Cai, J. M.; Algara-Siller, G.; Kaiser, U.; Weil, T.; Tzeng, Y. K.; Chang, H. C.; McGuinness, L. P.; Plenio, M. B.; Naydenov, B.; Jelezko, F. *Nano Lett.* **2013**, *13*, 3305−3309.
(20) Kaufmann, S.; Simpson, D. A.; Hall, L. T.; Perunicic, V.; Senn, P.; Steinert, S.; McGuinness, L. P.; Johnson, B. C.; Ohshima, T.; Caruso, F.; Wrachtrup, J.; Scholten, R. E.; Mulvaney, P.; Hollenberg, L. *Proc. Natl. Acad. Sci. U.S.A.* **2013**, *110*, 10894−10898.
(21) Grinolds, M. S.; Hong, S.; Maletinsky, P.; Luan, L.; Lukin, M. D.; Walsworth, R. L.; Yacoby, A. *Nat. Phys.* **2013**, *9*, 215−219.
(22) Rondin, L.; Tetienne, J. P.; Rohart, S.; Thiaville, A.; Hingant, T.; Spinicelli, P.; Roch, J. F.; Jacques, V. *Nat. Commun.* **2013**, *4*, 2279.

(23) Fu, C.-C.; Lee, H.-Y.; Chen, K.; Lim, T.-S.; Wu, H.-Y.; Lin, P.-K.; Wei, P.-K.; Tsao, P.-H.; Chang, H.-C.; Fann, W. *Proc. Natl. Acad. Sci. U.S.A.* **2007**, *104*, 727−732.

(24) Liu, K.-K.; Cheng, C.-L.; Chang, C.-C.; Chao, J.-I. *Nanotechnology* **2007**, *18*, 325102−325102.

(25) McGuinness, L. P.; Yan, Y.; Stacey, A.; Simpson, D. A.; Hall, L. T.; Maclaurin, D.; Prawer, S.; Mulvaney, P.; Wrachtrup, J.; Caruso, F.; Scholten, R. E.; Hollenberg, L. C. L. *Nat. Nano* **2011**, *6*, 358−363.

(26) Le Sage, D.; Arai, K.; Glenn, D. R.; DeVience, S. J.; Pham, L. M.; Rahn-Lee, L.; Lukin, M. D.; Yacoby, A.; Komeili, A.; Walsworth, R. L. *Nature* **2013**, *496*, 486−489.

(27) Hall, L. T.; Beart, G. C. G.; Thomas, E. A.; Simpson, D. A.; McGuinness, L. P.; Cole, J. H.; Manton, J. H.; Scholten, R. E.; Jelezko, F.; Wrachtrup, J.; Petrou, S.; Hollenberg, L. C. L. *Sci. Rep.* **2012**, *2*, 401.

(28) Kucsko, G.; Maurer, P. C.; Yao, N. Y.; Kubo, M.; Noh, H. J.; Lo, P. K.; Park, H.; Lukin, M. D. *Nature* **2013**, *500*, 54−58.

(29) Horowitz, V. R.; Alemán, B. J.; Christle, D. J.; Cleland, A. N.; Awschalom, D. D. *Proc. Natl. Acad. Sci. U.S.A.* **2012**, *109*, 13493−13497.

(30) Geiselmann, M.; Juan, M. L.; Renger, J.; Say, J. M.; Brown, L. J.; de Abajo, F. J. G.; Koppens, F.; Quidant, R. *Nat. Nano* **2013**, *8*, 175−179.

(31) Yi, C.; Li, C.-W.; Ji, S.; Yang, M. *Anal. Chim. Acta* **2006**, *560*, 1−23.

(32) Yun, H.; Kim, K.; Lee, W. G. *Biofabrication* **2013**, *5*, 022001.

(33) Steinert, S.; Ziem, F.; Hall, L. T.; Zappe, A.; Schweikert, M.; Götz, N.; Aird, A.; Balasubramanian, G.; Hollenberg, L.; Wrachtrup, J. *Nat. Commun.* **2013**, *4*, 1607.

(34) Micheal, A.; Satej, C.; Roland, P.; Shawn, W.; Benjamin, S. *Int. J. Robust Nonlinear Control* **2005**, *15*, 785−803.

(35) Cohen, A. E. *Phys. Rev. Lett.* **2005**, *94*, 118102.

(36) Chaudhary, S.; Shapiro, B. *Control Syst. Technol., IEEE Trans.* **2006**, *14*, 669−680.

(37) Komaee, A.; Shapiro, B. *Control Syst. Technol., IEEE Trans.* **2012**, *20*, 1011−1024.

(38) Nacev, A.; Komaee, A.; Sarwar, A.; Probst, R.; Kim, S. H.; Emmert-Buck, M.; Shapiro, B. *Control Syst., IEEE* **2012**, *32*, 32−74.

(39) Zhaolong, S.; Chen, K.; Shapiro, B. *Int. J. Optomechatronics* **2013**, *7*, 61−66.

(40) Ropp, C.; Probst, R.; Cummins, Z.; Kumar, R.; Berglund, A. J.; Raghavan, S. R.; Waks, E.; Shapiro, B. *Nano Lett.* **2010**, *10*, 2525−2530.

(41) Ropp, C.; Cummins, Z.; Probst, R.; Qin, S.; Fourkas, J. T.; Shapiro, B.; Waks, E. *Nano Lett.* **2010**, *10*, 4673−4679.

(42) Ropp, C.; Cummins, Z.; Nah, S.; Fourkas, J. T.; Shapiro, B.; Waks, E. *Nat. Commun.* **2013**, *4*, 1447.

(43) Bradac, C.; Gaebel, T.; Naidoo, N.; Sellars, M. J.; Twamley, J.; Brown, L. J.; Barnard, A. S.; Plakhotnik, T.; Zvyagin, A. V.; Rabeau, J. R. *Nat. Nano* **2010**, *5*, 345−349.

(44) Dréau, A.; Lesik, M.; Rondin, L.; Spinicelli, P.; Arcizet, O.; Roch, J. F.; Jacques, V. *Phys. Rev. B* **2011**, *84*, 195204.

(45) Toyli, D. M.; Christle, D. J.; Alkauskas, A.; Buckley, B. B.; Van de Walle, C. G.; Awschalom, D. D. *Phys. Rev. X* **2012**, *2*, 031001.

(46) Toyli, D. M.; de las Casas, C. F.; Christle, D. J.; Dobrovitski, V. V.; Awschalom, D. D. *Proc. Natl. Acad. Sci. U.S.A.* **2013**, *110*, 8417−8421.

(47) Trusheim, M. E.; Li, L.; Laraoui, A.; Chen, E. H.; Bakhru, H.; Schröder, T.; Gaathon, O.; Meriles, C. A.; Englund, D. *Nano Lett.* **2013**, *14*, 32−36.

(48) Andrich, P.; Alemán, B. J.; Lee, J. C.; Ohno, K.; de las Casas, C. F.; Heremans, F. J.; Hu, E. L.; Awschalom, D. D. *Nano Lett.* **2014**, *14*, 4959−4964.

(49) Dolde, F.; Fedder, H.; Doherty, M. W.; Nobauer, T.; Rempp, F.; Balasubramanian, G.; Wolf, T.; Reinhard, F.; Hollenberg, L. C. L.; Jelezko, F.; Wrachtrup, J. *Nat. Phys.* **2011**, *7*, 459−463.

Scanning localized magnetic fields in a microfluidic device with a single nitrogen vacancy center

Kangmook Lim, Chad Ropp, Benjamin Shapiro, Jacob M. Taylor, Edo Waks

Supporting Information

Fluid composition

   The fluid solution is composed of 1.5 wt % rheology modifier (Acrysol RM-825, Rohm and Haas Co.) and 2.5 % by volume ethoxylated-15 trimethylolpropane triacrylate resin (SR-9035, Sartomer) in deionized water. The rheology modifier is used to increase viscosity of the fluid to reduce Brownian motion of the magnetic particles, and the triacrylate resin creates a fluid chemistry that pushes the magnetic particles to the top PDMS surface of the microfluidic channels.

Optical measurement setup

   We mount the microfluidic device on an inverted confocal microscope system that excites and collects emission from a NV center and images a manipulated magnetic particle through the bottom glass cover slip using a 1.45 numerical aperture oil immersion objective. A piezo stage attached to the microscope enables precise translation of the microfluidic device in three dimensions. We excite the NV center using a 532 nm continuous wave laser and use a half-

waveplate to rotate the polarization to achieve maximum fluorescence intensity. In addition to the excitation laser, we use a white light source to image the magnetic particle. The excitation laser beam is tightly focused onto the NV center while the white light beam is widely focused to a 20 μm diameter.

A beamsplitter sends 25% of the collected light to an EM-CCD camera (Hamamatsu C9100-13) to track the magnetic particle using a 10 Hz camera frame rate. The remaining 75% of the collected light is spatially filtered by a pinhole aperture and is spectrally filtered using a 600-750 nm bandpass filter. This combination of spatial and spectral filtering isolates the emission from the NV center and rejects the background signal from the scattered white light with a high extinction ratio. The filtered NV emission is directed to an avalanche photodiode (PerkinElmer SPCM-AQR) to perform optically detected ESR measurements. The signal can also be directed to a Habury-Brown Twiss (HBT) intensity interferometer composed of a 50/50 beam-splitter and two avalanche photodiodes, to perform second order correlation measurements. A time interval analyzer (PicoQuant PicoHarp 300) performs time-resolved coincidence detection using the outputs of the two photon counters.

Feedback flow control system

Details of the microfluidic control system have been reported in[1-3]. The EM-CCD camera continuously monitors the position of a selected magnetic particle to nanoscale accuracy using sub-pixel averaging. The feedback control algorithm compares the current position of the particle with the desired position and applies voltages at the four ends of the microfluidic channels using platinum electrodes. These voltages then induce a corrective electroosmotic flow that moves the suspended magnetic nanoparticle from its current position to its desired position

by viscous drag. This process continuously moves the particle as desired with nanoscale accuracy. This method enables two-dimensional control of a suspended magnetic particle in the microfluidic channel in real time.

ESR spectrum using Digital lock-in approach

We take ESR spectra of an NV center using a digital lock-in approach while a magnetic nanoparticle is held at desired position. We modulate the microwave signal generator on and off at a 1 KHz rate and calculate the photoluminescence intensity contrast using the measured photon counts synchronized with the modulation. We run a sequence of frequency sweeps with frequency steps of 1 MHz and integration times of 0.1 sec and integrate the data over the time windows. Thus the data points at each frequency in Figure 3 are composed of photon counts that have been integrated over 25 data runs that are separated by 10 sec time intervals. There are 100 frequency steps in the entire spectrum, which leads to a 250 sec integration time per ESR spectrum. In the experimental run we report here, we obtained 12 ESR spectra at different magnetic particle distances from the NV center which leads to a total measurement time of 50 minutes.

Shot noise limited fluctuations

We estimate photoluminescence intensity fluctuation due to shot noise using the equation

$$\partial C^2 = \left(\frac{\partial C}{\partial N_{on}} \right)^2 \partial N_{on}^2 + \left(\frac{\partial C}{\partial N_{off}} \right)^2 \partial N_{off}^2 \qquad (1)$$

In the shot noise limit, $\partial N_{on}^2 = N_{on}$ and $\partial N_{off}^2 = N_{off}$. Using Equation 1 of the main manuscript, and the fact that in our measurements $N_{on} \approx N_{off}$, we attain

$$\partial C = \sqrt{\frac{2}{N_{off}}} \; . \tag{1}$$

For the data in Fig. 3a, we have $N_{off} = 56250$, obtained the count rate of 45 kCts/s and 1.25s integration time, which corresponds to $\partial C = 0.6\%$.

Fitting measured magnetic field to theoretical dipole model

We assume the magnetic particle behaves like a magnetic dipole whose magnetic field is given by

$$\mathbf{B}_{dip} = \frac{\mu_0}{4\pi} \frac{3\mathbf{r}(\mathbf{m}\cdot\mathbf{r}) - mr^2}{r^5} \; , \tag{3}$$

where μ_0 is the vacuum permeability and the magnetic moment of the dipole $\mathbf{m}$ points orthogonal to the microfluidic device surface. The magnetic field measured by the NV center is the projection of the magnetic field of the dipole $\mathbf{B}_{dip}$ onto the NV orientation $\boldsymbol{\beta}$:

$$B_{NV} = \boldsymbol{\beta} \cdot \mathbf{B}_{dip} \; . \tag{4}$$

We fit B_{NV} to the measured data points using $|\mathbf{m}|$ and $\boldsymbol{\beta}$ as fitting parameters.

1.	Ropp, C.; Probst, R.; Cummins, Z.; Kumar, R.; Berglund, A. J.; Raghavan, S. R.; Waks, E.; Shapiro, B., Manipulating Quantum Dots to Nanometer Precision by Control of Flow. *Nano Letters* 2010, 10, 2525-2530.
2.	Ropp, C.; Cummins, Z.; Probst, R.; Qin, S.; Fourkas, J. T.; Shapiro, B.; Waks, E., Positioning and Immobilization of Individual Quantum Dots with Nanoscale Precision. *Nano Letters* 2010, 10, 4673-4679.

3.   Ropp, C.; Cummins, Z.; Nah, S.; Fourkas, J. T.; Shapiro, B.; Waks, E., Nanoscale imaging and spontaneous emission control with a single nano-positioned quantum dot. *Nat Commun* 2013, 4, 1447.